International Journal of Multiphase Flow 202 (2026) 105823

Contents lists available at ScienceDirect

International Journal of Multiphase Flow

journal homepage: www.elsevier.com/locate/ijmulflow

Research Paper

Volume-averaged two-phase simulation for predicting rheological behavior in dense suspensions

A. Ludwig *, C. Gomes Rodrigues, M. Stefan-Kharicha, M. Wu, A. Kharicha

Metallurgy Department, Technical University Leoben, Austria

HIGHLIGHTS

- A two-phase volume-averaged model is proposed that accounts for the effect of the particle pressure in dense suspensions.
- Its application to a rotational annulus shear cell rheometer enables the prediction of process details that would otherwise remain obscure and clarifies the conditions under which commonly made simplifying assumptions are justified.
- A high shear rate at the upper outer edge of the shear cell induces an axial-radial flow from smaller to larger radii, superimposed on the global rotational flow. This axial-radial flow may get weak for solid fractions close to the packing limit.
- The scaling of particle pressure and shear stress with the shear rate allows for correct measurements of the friction coefficient and the dimensionless viscous number, even when the numerically estimated shear rates deviate substantially from the values considered in the experiments.

GRAPHICAL ABSTRACT

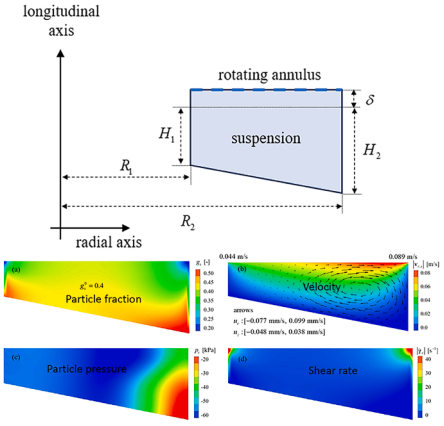

ARTICLE INFO

Keywords:
Rheology
Suspension
Particle pressure
Volume-averaged multiphase model
Process simulation

ABSTRACT

A two-phase volume-averaged model is proposed that accounts for the effect of the particle pressure in dense suspensions. Although the predictions of the model can only be regarded as approximations to reality, its application to a rotational annulus shear cell rheometer enables the prediction of process details that would otherwise remain obscure and clarifies the conditions under which commonly made simplifying assumptions are justified. It was shown that a high shear rate at the upper outer edge of the shear cell induces an axial-radial flow from smaller to larger radii, superimposed on the global rotational flow. This flow transports particles from the regions beneath the annulus towards the bottom. Consequently, the friction coefficient and the dimensionless viscosity number depend on the applied rotation speed. This dependence diminishes when the strength of axial-

* Corresponding author at: Technical University of Leoben, Austria
E-mail address: ludwig@unileoben.ac.at (A. Ludwig).

https://doi.org/10.1016/j.ijmultiphaseflow.2026.105823
Received 30 March 2026; Received in revised form 23 June 2026; Accepted 26 June 2026
Available online 2 July 2026

radial flow is negligibly small, and no particle redistribution occurs, which may happen at sufficiently high particle volume fraction. The linear scaling of particle pressure and shear stress with shear rate enables the determination of the friction coefficient and the dimensionless viscosity number, even when the considered shear rates differ substantially from the experimental approximations. The simulations indicate that, in the corresponding experiments, the actual shear rate may be several times larger than predicted by the commonly used oversimplified assumption.

1. Introduction

Volume-averaged multiphase simulations of alloy solidification have become increasingly common for predicting microstructure formation and evaluating the occurrence and severity of macrosegregation in large castings (Cai et al., 2019; Combeau and Založnik, 2014; Ge et al., 2018; Gu and Beckermann, 1999; Heyvaert et al., 2017; Ludwig et al., 2014; Wu et al., 2018; Založnik and Combeau, 2010). Particularly when the formation and movement of equiaxed crystals are crucial, this method is unparalleled due to its ability to handle a large number of small, moving solid particles (Combeau et al., 2009; Leriche et al., 2015; Li et al., 2014; Nguyen et al., 2018, 2015; Wu et al., 2017). It pertains to the idea of multiphase systems, where multiple phases (gas, liquid, or solid) coexist within a certain volume. The phases are well-mixed but spatially distinct from each other. The macroscopic conservation equations for each phase are derived by averaging the microscopic (exact) equations over specified averaging volumes, which typically correspond to the volumes of a numerical grid (Dantzig and Rappaz, 2016; Ni and Beckermann, 1991). The volume-averaged conservation equations for mass, momentum, energy, and concentration are formulated for each of the phases considered. In the context of the momentum conservation equation, the volume-averaged shear stress term is typically described using the standard constitutive laws for incompressible fluids,

$$\boldsymbol{\tau}_i = \eta_i \dot{\gamma}_i \text{ with } \dot{\gamma}_i = \left[\nabla \mathbf{v}_i + (\nabla \mathbf{v}_i)^T\right] \text{for } i = 1, \ldots, n \tag{1}$$

where $\boldsymbol{\tau}_i$ represents the shear stress tensor, $\dot{\gamma}_i$ denotes the shear rate tensor, and $\mathbf{v}_i$ corresponds to the flow velocity of the phases, $i = 1,\ldots,n$. All quantities are considered to be volume-averaged. The effective macroscopic shear viscosity, η_i, is generally derived from the microscopic counterpart. This choice works well for gases and liquids. However, for particulate systems where solid particles move within a fluid, the effective solid viscosity, η_s, is chosen such that the mixture properties are accurately represented. At this point, experimental findings from the rheology community are generally adopted in the solidification community. A widely used approach, derived from experimental results on monodisperse latices, is the well-known Krieger-Dougherty expression (Krieger, 1972; Krieger and Dougherty, 1959) describing the dependence of the mixture viscosity, η_{mix}, on solid fraction, g_s,

$$\eta_{\text{mix}} = \eta_\ell^0 \left(1 - \frac{g_s}{g_s^c}\right)^{-2.5 g_s^c} \tag{2}$$

where g_s^c denotes the solid volume fraction at which the data diverges, and η_ℓ^0 the viscosity of the liquid phase in the absence of solid particles. Applying the mixture rule $\eta_{\text{mix}} = g_\ell \eta_\ell + g_s \eta_s$ then leads to the following expression for the effective solid viscosity,

$$\eta_s = \frac{\eta_\ell^0}{g_s}\left(\left(1 - \frac{g_s}{g_s^c}\right)^{-2.5 g_s^c} - (1 - g_s)\right). \tag{3}$$

This approach was first proposed in the pioneering work of Ni and Beckermann (1993) on multiphase volume-averaged solidification modelling and has since been applied in numerous subsequent studies of equiaxed solidification (Ge et al., 2018, 2017; Li et al., 2014; Ludwig and Wu, 2002; Ren et al., 2018; Wang et al., 2020; Wu et al., 2010a, 2010b; Wu and Ludwig, 2009a, 2009b). The present authors are therefore particularly interested in assessing the validity and generality of this expression, as well as of the underlying volume-averaged approach.

In their review paper (Guazzelli and Pouliquen, 2018), Guazzelli and Pouliquen compiled experimental data from a range of rheological studies, as presented in their Fig. 4. It was shown that all η_{mix}vs. $g_s$curves follow a similar trend, with Krieger's curve (Eq. 2) lying slightly below the others. Among the analyzed data sets, two originate from the experimental study by Boyer et al. (Boyer et al., 2011). Since the present study applies a volume-averaged two-phase approach to their experiments, the following discussion focuses on their results.

Boyer et al. (2011) performed rheological measurements using an annular shear cell. In this setup, a suspension of solid spheres in a Newtonian liquid was confined between a stationary truncated cone and a rotating annulus (Fig. 1). The annulus was semi-permeable and allowed to move vertically. The experimental inputs were the torque, M_B, and the force, F_B, applied by the rotating annulus to the suspension. The measurements recorded the resulting rotational speed, ω, and the vertical displacement of the annulus, δ, once quasi steady-state conditions were reached. Initially, the suspension had a solid volume fraction of g_{s0}, with the annulus positioned at $\delta = 0$ under zero normal force. From the measured M_B and F_B, the shear stress, $\tau_B = 3M_B/2\pi\left(R_2^3 - R_1^3\right)$, and the particle pressure, $P_B = F_B/\pi\left(R_2^2 - R_1^2\right)$, were calculated. Here, R_1 and R_2 denote the inner and the outer radius of the rheometer, respectively, as indicated in Fig. 1. The particle pressure is also called granular or contact pressure.

The resulting solid volume fraction was calculated from the measured δ as $g_s = g_{s0}/(1 + f(\delta))$, where $f(\delta) = \left[3R_2\left(R_2^2 - R_1^2\right)\delta\right]/\left[2\left(R_2^3 - R_1^3\right)H_2\right]$ was obtained from straightforward geometrical considerations, as outlined by Boyer et al. (2011). Assuming that the shear rate was approximately uniform in the vertical and radial directions, a simple relationship between the mean shear rate, averaged across the annulus, and ω was applied: $\dot{\gamma}_B = \langle \omega r / h(r) \rangle = \omega R_1 / H_1$. This approximation was justified by the choice of a conical bottom plate, such that the ratio of radius to height remains constant, $r/h(r) = R_1/H_1 = R_2/H_2$.

The authors found that dense suspensions containing spherical particles of equal size can be fully characterized by the evolution of two quantities: the friction coefficient, $\mu = \tau/P^p$, and the dimensionless viscous number, $I_v = \eta_\ell^0 \dot{\gamma}/P^p$ (Boyer et al., 2011). Using these two

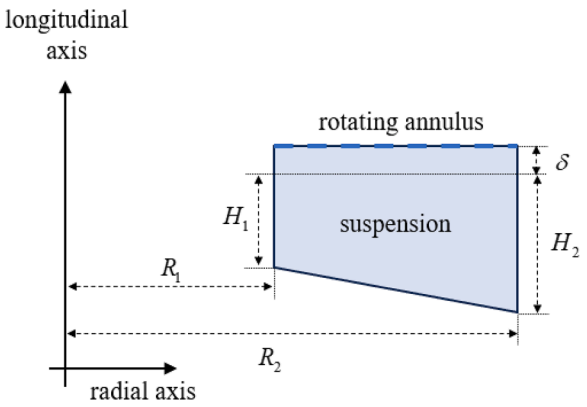

Fig. 1. Schematic of the numerical domain representing the experiment from Boyer et al. (2011) in cylindrical coordinates. The azimuthal coordinate is not shown. In three dimensions, the domain forms a ring with a conical lower boundary. Only the top cover rotates.

quantities, the shear stress, τ, and the particle pressure, P^p, can be expressed as functions of the shear rate, $\dot{\gamma}$, as follows:

$$\tau = \mu P^p = \eta_\ell^0 \frac{\mu}{I_v}\dot{\gamma} = \eta_\ell^0 \eta_s \dot{\gamma}, \tag{4}$$

and

$$P^p = \eta_\ell^0 \frac{1}{I_v}\dot{\gamma} = \eta_\ell^0 \eta_n \dot{\gamma}, \tag{5}$$

where $\eta_s = \mu/I_v$ is the dimensionless shear viscosity, and $\eta_n = 1/I_v$ is the dimensionless normal viscosity of the suspension. For μ and I_v, they suggested the following relationships:

$$\mu(g_s) = \underbrace{\mu_1 + \frac{\mu_2 - \mu_1}{1 + I_0 \Big/ \left(\frac{g_{s,c} - g_s}{g_s}\right)^2}}_{=\mu_c} + \underbrace{\left(\frac{g_{s,c} - g_s}{g_s}\right)^2 + \mu_3 g_{s,c}\left(\frac{g_{s,c} - g_s}{g_s}\right)}_{=\mu_h}, \tag{6}$$

and

$$I_v(g_s) = \left(\frac{g_{s,c} - g_s}{g_s}\right)^2. \tag{7}$$

As empirical quantities, they used $\mu_1 = 0.32$, $\mu_2 = 0.7$, $\mu_3 = 2.5$, and $I_0 = 0.005$. The quantitiesμ_c and μ_h were identified as the contact friction coefficient and the hydrodynamic contribution to the friction coefficient. The solid volume fraction at which the viscosity of the suspension diverges was found to be$g_{s,c} = 0.585$.

To date, multiphase volume-averaged solidification models have overlooked the contribution of particle pressure. In the present study, we have modified a two-phase volume-averaged approach to incorporate this additional pressure effect. This work aims to numerically reproduce the rheological experiments of Boyer et al. (2011) and to investigate the conditions under which their unique relationships, $\mu(g_s)$and $I_v(g_s)$, Eqs. (6–7) are valid.

2. Numerical model

In pressure-imposed rheometers, the suspension is confined between a fixed lower plate and a porous top plate, which permits fluid flow while restricting particle movement. The top plate rotates to shear the suspension at a constant rate, while remaining free to move vertically. Its final height is determined by the balance between an externally applied, constant vertical force and the dilatation or compressive force arising from the particle pressure. This configuration enables the measurement of particle pressure from the position of the top plate.

In volume-imposed rheometers, the suspension is confined between two plates, with the distance between them held constant. As a result, the suspension is sheared at a defined shear rate while maintaining a global volume fraction. In this configuration, the particle pressure varies in response to both the shear rate and volume fraction, and can be determined from the total pressure in the system. In summary, for the pressure-imposed rheology, M_B and F_B are the input parameters, while ω and g_s (as a function δ) are the output quantities. In contrast, for the volume-imposed rheology, the roles are reversed, with ω and g_s serving as the input parameters, and M_B and F_B as the output quantities.

Initially, an attempt was made to simulate the flow within the domain using a semi-permeable top plate, which could move vertically in response to the particle pressure exerted on it. While this approach yielded some promising results, the numerical code proved unstable and lacked the flexibility to accommodate variations in the process parameters across a wide range. Therefore, the modeling approach was reformulated using a volume-imposed configuration, in which the global solid volume fraction is prescribed and the particle pressure emerges as part of the solution. While pressure-imposed and volume-imposed rheological descriptions can be related through constitutive frameworks (Guazzelli and Pouliquen, 2018), their equivalence is not guaranteed a priori for spatially non-uniform flows such as the present case. In the following, it is assumed that the volume-imposed formulation captures the dominant steady-state mechanisms governing shear-induced particle migration and stress development in the system.

For the process under consideration, under steady-state conditions, both phases exhibit nearly identical velocity and shear stress fields; hence, no distinction between the volume-averaged velocity, shear rate, and shear stress of the liquid and solid phases is requested. To enable the comparison against Boyer's experimental data, M_B and F_B were determined by evaluating the mean values acting at the cover surface as

$$\overline{\tau}_{surf} = \frac{1}{\pi(R_2^2 - R_1^2)} \int_{R_1}^{R_2}\int_0^{2\pi} |\boldsymbol{\tau}|\cdot dA \quad \Rightarrow \quad M_B = \overline{\tau}_{surf}\cdot\frac{2}{3}\pi\left(R_2^3 - R_1^3\right), \tag{8}$$

and

$$\overline{p}_{c,surf} = \frac{1}{\pi(R_2^2 - R_1^2)} \int_{R_1}^{R_2}\int_0^{2\pi} p_c(r)\cdot dA \quad \Rightarrow \quad F_B = \overline{p}_{c,surf}\cdot\pi\left(R_2^2 - R_1^2\right). \tag{9}$$

The mean value of the shear rate at the annulus was evaluated by

$$\overline{\dot{\gamma}}_{surf} = \frac{1}{\pi(R_2^2 - R_1^2)} \int_{R_1}^{R_2}\int_0^{2\pi} |\dot{\gamma}|\cdot dA. \tag{10}$$

In addition, we have estimated the volumetric mean values of τ,$p_c$and $\dot{\gamma}$ by

$$\overline{\tau}_{vol} = \frac{1}{Vol}\int_{Vol} |\boldsymbol{\tau}| dv, \tag{11}$$

and

$$\overline{p}_{c,Vol} = \frac{1}{Vol}\int_{Vol} p_c dv. \tag{12}$$

and

$$\overline{\dot{\gamma}}_{vol} = \frac{1}{Vol}\int_{Vol} |\dot{\gamma}| dv. \tag{13}$$

where the integration was done over the entire suspension volume. The importance of these quantities will be discussed below.

In the pressure-imposed rheometer, the force acting on the annulus, F_B, interacts solely with the particles, as the liquid can flow freely through the holes in the permeable annulus. This is different for the volume-imposed rheometer, where F_B also includes contributions from both the liquid and the particles, due to the constraint of constant volume. As a result, the volume-fraction weighted pressure field (mixture pressure) is given by $P_{mix} = g_\ell p_\ell + g_s p_s = p_c + p_\ell$, where a particle pressure, P^p, has been defined as $P^p = p_c = g_s(p_s - p_\ell)^*$. p_ℓ and p_s are the volume-averaged fluid and particle pressure. To compare our volume-imposed simulation results against the pressure-imposed rheometer measurements, only p_c is used to evaluate Eqs. (9), (12), and to calculate the force corresponding to the measurements.

The annular shear rheometer used in the simulation is identical to the one described by Boyer et al. (2011) with dimensions R_1= 0.044 m, R_2= 0.09 m, H_1= 0.0088 m, and H_2= 0.018 m (Fig. 1). The total volume of the ring-shaped domain is given by $V_0 = \frac{2}{3}\pi\left(R_2^3 - R_1^3\right)H_2/R_2$, resulting in

* The relevance of this definition will become obvious in the text around Eq. (20).

a value of V_0[†]$= 269.68$ cm^3. The applied boundary conditions are detailed in Table 1. Note that in the experiment, both the bottom and top plates were modified by gluing 0.5 mm steel bars radially, spaced 5 mm apart. As a result, both the liquid and solid phases were essentially forced to adhere to the bottom and top surfaces. This was considered in the simulation by using the corresponding boundary condition.

Since the simulations were set up as a quasi-time-dependent problem, the suspension was assumed to be at rest, with a uniform solid fraction as the initial condition. A simulation was run until steady-state results were achieved. Following the information given in Boyer et al. (2011), we considered two sets of suspensions: monodispersed spheres with a diameter $d= 0.58$ mm in a liquid with $\eta_f^0= 2.15$ Pa·s, and $d= 1.1$ mm in a liquid with $\eta_f^0= 3.1$ Pa·s.

2.1. Volume-averaged two-phase equations

As volume-averaged mass and momentum conservation equations, the following expressions were applied (Ahnert et al., 2019; Ni and Beckermann, 1991)

$$\frac{\partial(g_\ell\rho_\ell)}{\partial t}+\nabla\cdot(g_\ell\rho_\ell\mathbf{v}_\ell)=0, \tag{14}$$

$$\frac{\partial(g_s\rho_s)}{\partial t}+\nabla\cdot(g_s\rho_s\mathbf{v}_s)=0, \tag{15}$$

$$\frac{\partial(g_\ell\rho_\ell\mathbf{v}_\ell)}{\partial t}+\nabla\cdot(g_\ell\rho_\ell\mathbf{v}_\ell\otimes\mathbf{v}_\ell)=-\nabla(g_\ell p_\ell)+\nabla\cdot(g_\ell\boldsymbol{\tau}_\ell)-\mathbf{M}+g_\ell\rho_\ell\mathbf{g}+\overline{p}_{\ell i}\nabla g_\ell, \tag{16}$$

$$\frac{\partial(g_s\rho_s\mathbf{v}_s)}{\partial t}+\nabla\cdot(g_s\rho_s\mathbf{v}_s\otimes\mathbf{v}_s)=-\nabla(g_s p_s)+\nabla\cdot(g_s\boldsymbol{\tau}_s)+\mathbf{M}+g_s\rho_s\mathbf{g}+\overline{p}_{si}\nabla g_s. \tag{17}$$

Here $\otimes$ denotes the (direct) dyadic product, ρ_ℓ and ρ_s are the fluid and particle densities (assumed constant and equal), $\mathbf{v}_\ell$ and $\mathbf{v}_s$ the volume-averaged fluid and particle velocity fields, p_ℓ and p_s the volume-averaged pressure fields in the fluid and the particles, $\boldsymbol{\tau}_\ell$and $\boldsymbol{\tau}_s$ the volume-averaged deviatoric stress tensors, $\mathbf{g}$ the gravitational acceleration vector and $\mathbf{M}$ the vector that contains the dissipative interfacial forces due to viscous and form drag and unbalanced pressure distributions leading to lift and virtual mass (acceleration) effects. In Ahnert et al. (2019), the body force due to gravity was ignored.

The volume-averaged interface pressures, $\overline{p}_{\ell i}$ and $\overline{p}_{si}$, are generally taken as p_ℓ. For the volume-averaged phase pressures $p_s \neq p_\ell$ must be assumed, especially when a coherent solid network with interstitial liquid exists, as for late solidification (Farup and Mo, 2000; Martin et al., 2002, 1999, 1997a, 1997b; Nguyen et al., 1994) or when particles in a suspension are frequently in contact (Ahnert et al., 2019; Boyer et al., 2011). Only when particles are mainly surrounded by liquid $p_s = p_\ell$ is justified. This is often assumed in the solidification community (Combeau et al., 2009; Heyvaert et al., 2017; Li et al., 2014; Nguyen et al., 2018, 2015; Ni and Beckermann, 1991; Wu and Ludwig, 2009a). What has been said leads to[‡]

$$-\nabla(g_\ell p_\ell)+\overline{p}_{\ell i}\nabla g_\ell=-g_\ell\nabla p_\ell \tag{18}$$

and

$$-\nabla(g_s p_s)+\overline{p}_{si}\nabla g_s=-g_s\nabla p_\ell-\nabla(g_s(p_s-p_\ell)). \tag{19}$$

The second term on the right-hand side of Eq. (19) is the gradient of the (weighted) solid contact pressure (Ahnert et al., 2019), which is considered in this study as particle pressure,

$$P^p=p_c=g_s(p_s-p_\ell). \tag{20}$$

With Eqs. (18), (19), and (20), the volume-averaged momentum conservation equations, Eqs. (16) and (17), can be expressed as

$$\frac{\partial(g_\ell\rho_\ell\mathbf{v}_\ell)}{\partial t}+\nabla\cdot(g_\ell\rho_\ell\mathbf{v}_\ell\otimes\mathbf{v}_\ell)=-g_\ell\nabla p_\ell+\nabla\cdot(g_\ell\boldsymbol{\tau}_\ell)-\mathbf{M}+g_\ell\rho_\ell\mathbf{g}, \tag{21}$$

$$\frac{\partial(g_s\rho_s\mathbf{v}_s)}{\partial t}+\nabla\cdot(g_s\rho_s\mathbf{v}_s\otimes\mathbf{v}_s)=-g_s\nabla p_\ell-\nabla p_c+\nabla\cdot(g_s\boldsymbol{\tau}_s)+\mathbf{M}+g_s\rho_s\mathbf{g}. \tag{22}$$

Neglecting lift and virtual mass effects for simplicity, the dissipative interfacial force $\mathbf{M}$ might be considered only the momentum transfer on drag, for which the often-used Kozeny-Carman law is applied[§].

$$\mathbf{M}=\mathbf{M}^{drag}=\frac{\eta_\ell^0 g_s^2}{K_p(1-g_s)}(\mathbf{v}_\ell-\mathbf{v}_s)\ \text{with}\ K_p=\frac{d^2}{180}. \tag{23}$$

Although it was found that under steady-state conditions, both phases move at nearly the same velocity, differences in the drag coefficient alter the velocity gradients, which can lead to, for example, different solid fraction distributions.

For the solid contact pressure, Ni and Beckermann (1991) assumed equal volume-averaged pressure fields in the fluid and the particles, $p_s = p_\ell$, and according to Eq. (20) no particle pressure, $p_c = 0$. In contrast, Ahnert et al. (2019) assumed an isotropic solid contact pressure by applying Eq. (20) in their two-phase model. As outlined in Guazzelli and Pouliquen (2018), the particle pressure may be non-isotropic, particularly in rotating flow configurations, and the particle pressure term in Eq. (22) can, in its simplest form, be expressed as:

$$\nabla p_c\rightarrow\nabla\cdot\boldsymbol{\sigma}^p=\nabla\cdot\left(\eta_{\text{norm}}\eta_\ell|\dot{\gamma}_s|\begin{pmatrix}1&0&0\\0&\lambda_2&0\\0&0&\lambda_3\end{pmatrix}\right). \tag{24}$$

For curvilinear shear flows, the coefficients were found to be $\lambda_2\approx 0.8$and $\lambda_3\approx 0.5$ (Morris and Boulay, 1999). We have applied this concept to the experiment of Boyer et al. (2011), considering that the diagonal coefficients $1, \lambda_2, \lambda_3$ are related to the cylindrical coordinates r, z, φ. For evaluating p_c in Eqs. (9) and (12), the corresponding axial z-component was used. Note that while an isotropic assumption was initially considered, preliminary simulations indicated that a simplified isotropic model struggled to maintain stable numerical convergence near the sharp gradients of the probe. Consequently, the anisotropic formulation was adopted as a practical modeling approach to ensure stable flow solutions. The coefficients in the anisotropic closure (taken from Morris and Boulay, 1999) are treated as phenomenological parameters and are not independently calibrated for the present system.

Numerical implementation

For the simulations presented below, we have solved Eqs. (14), (15),

Table 1
Applied boundary conditions.

	Liquid phase	Solid phase
Inner radius	no-slip	slip
Outer radius	no-slip	slip
Bottom	no-slip	no-slip
Rotating top annulus	ω	ω

[†] (Boyer et al., 2011) got $V = 255$ cm^3, although using the same data and formula.

[‡] Note that Eq. (24d) in (Ahnert et al., 2019) uses $\overline{p}_{li}\nabla g_s$instead of $\overline{p}_{si}\nabla g_s$for our Eq. (17). This is still consistent with the present description as it is assumed that $\overline{p}_{\ell i}\simeq\overline{p}_{si}$anyway.

[§] The factor 180 was not explicitly mentioned in (Ahnert et al., 2019) but can be seen as standard.

(21), (22) with Eq. (23) and the closure relations Eqs. (1), (3), and (24) to get the volume-averaged values for g_s,$\mathbf{v}_\ell$,$\mathbf{v}_s$ and p_ℓ. The numerical simulations were performed in Ansys Fluent, version 19.2. To accurately capture the interaction between the phases within the suspension, a multiphase Euler-Euler model was adopted. This framework treats both the liquid and solid phases as interpenetrating continua, solving a set of momentum and continuity equations for each phase.

To reduce computational cost, a 2D axisymmetric swirl formulation was used to represent the rheometer geometry. The swirl velocity was prescribed as a fixed rotational field, corresponding to a constant angular velocity imposed at the top surface. The additional source term corresponding to Eq. (24) was implemented via user-defined functions (UDFs) and hooked to the momentum equation of the solid phase. The computational domain was discretized using a structured mesh consisting of 4000 quadrilateral cell elements, with an average cell size of approximately 0.4 mm.

Temporal discretization was performed using a fixed time step of 0.001 s. Each time step allowed a maximum of 40 inner iterations to achieve convergence of the coupled pressure-velocity system. Convergence at each time-step was assessed using Fluent's default residual criteria, with all monitored residuals (continuity, momentum, and volume fraction) required to fall below a threshold of 1×10^{-3}.

The model employed in the present study has been previously validated against two benchmark experimental datasets commonly used to assess shear-induced particle migration models. The first is the channel flow experiments of Lyon and Leal (1998) who measured particle concentration and velocity profiles across a two-dimensional channel for concentrated suspensions at varying flow rates and bulk volume fractions. The second is the Couette flow experiments of Phillips et al. (199), who documented shear-induced particle migration in a wide-gap Couette device and proposed a constitutive framework based on gradients in shear rate and viscosity. In both cases, the driving mechanism for particle redistribution is the spatial variation of particle shear stresses, leading to migration from regions of high to low shear. Detailed comparisons of particle concentration and velocity profiles, showing good agreement with experimental data, are reported in Ludwig et al. (2020). Specifically, for the two-dimensional channel flow benchmark ($g_s^0 = 0.4$), the model successfully captured the inhomogeneous particle accumulation along the centerline (predicting a peak solid fraction of approx 0.52). For the wide-gap Couette flow benchmark ($g_s^0 = 0.55$), the model closely matched the measured radial migration after 200 revolutions, predicting a drop in solid fraction to about 0.35 at the rotating inner cylinder and a corresponding build-up to approximately 0.58 at the stationary outer wall. The present work builds on this validated framework. Since the main focus of the present work is not on model validation but on the analysis of flow and particle redistribution in an annular shear cell, these benchmark results are not repeated here.

3. Results

As outlined above, both the pressure-imposed and the volume-imposed rheological shear cell experiments establish a relationship between the shear stress τ, the particle pressure P^p, the rotation speed ω, and the applied solid volume fraction g_s^0.

For our simulations, we varied g_s^0 in the range from 0.30 to 0.56 and ω in the range from 1 rad/s ($0.16\ s^{-1} \approx 9.5$ rpm) to 125 rad/s ($19.9\ s^{-1} \approx 1187$ rpm). Boyer et al. conducted their experiments over the same range of solid volume fraction, but with ω ranging from 0.13 rad/s ($0.02\ s^{-1} \approx 1.2$ rpm) to 2.5 rad/s ($0.4\ s^{-1} \approx 24$ rpm) (Boyer et al., 2011). Thus, our simulations encompass their process window, while extending it to a significantly larger ω.

The relevant values of τ, P^p, and $\dot{\gamma}$ were determined numerically from mean quantities obtained by surface integration immediately beneath the annulus, $\overline{\tau}_{surf}$, $\overline{p}_{c,surf}$, and $\overline{\dot{\gamma}}_{surf}$, Eqs. (8–10), and, alternatively, by volume integration, $\overline{\tau}_{vol}$, $\overline{p}_{c,Vol}$, and $\overline{\dot{\gamma}}_{vol}$, Eqs. (11–13). $\overline{\tau}_{surf}$ and $\overline{\tau}_{vol}$, although different in magnitude, ranged from 80 Pa to 44 kPa, while $\overline{p}_{c,surf}$ and $\overline{p}_{c,Vol}$ from 50 Pa to 37 kPa.

Fig. 2 shows $\overline{\dot{\gamma}}_{surf}$, $\overline{\dot{\gamma}}_{vol}$ and $\dot{\gamma}_B = \langle \omega r / h(r) \rangle = \omega R_1 / H_1$ as function ω. It turned out that also $\overline{\dot{\gamma}}_{surf}$ and $\overline{\dot{\gamma}}_{vol}$ increase linearly with ω, with values ranging from approximately 6 s^{-1} to 1800 s^{-1}, and $\overline{\dot{\gamma}}_{surf}$ being approximately 2.4 times larger than $\overline{\dot{\gamma}}_{vol}$, and approximately 16–17 times larger than $\dot{\gamma}_B$.

Fig. 3 presents an example of a simulation result in which the particle pressure is analysed after steady-state conditions have been established. The process conditions involve spherical particles with a diameter of d= 0.58 mm, suspended in a liquid with a viscosity of $\eta_\ell^0 = 2.15$ Pa s, and subjected to a rotation speed of $\omega = 1$ rad/s ($0.16\ s^{-1} \approx 9.5$ rpm). The shear cell was initially filled uniformly with a solid volume fraction of g_s^0= 0.40.

In contrast to the considerations presented in Boyer et al. (2011), the model predicts several unexpected behaviors (Fig. 3). First, the simulated solid volume fraction is not uniform: particles are shown to accumulate in the lower corners and are depleted in the upper corners. In addition to the imposed rotation, the model predicts the development of a clockwise flow on the axial-radial plane, as indicated by the arrows. The simulated particle pressure is likewise non-uniform, exhibiting its lowest absolute values in the lower outer corner and highest absolute values along the vertical centreline of the domain. Finally, the simulated shear rate shows markedly elevated values in the upper corners, while remaining approximately uniform throughout the bulk of the domain.

Fig. 4 presents the friction coefficient, μ, and the dimensionless viscous number, I_V, as functions of the initial solid volume fraction g_s^0. In addition to the curves derived from Eqs. (6–7), the results of several numerical cases are shown. A distinction is again made between values determined by surface integration and those obtained by volume integration. Evidently, the values derived from the volume integration are more consistent with the findings of Boyer et al., whereas those obtained from the surface integration exhibit noticeable deviations.

For both plots in Fig. 4, it can be observed that the higher the rotation speed, the closer the values of μ and I_V, determined from $\overline{\dot{\gamma}}_{surf}$ and $\overline{p}_{c,surf}$, are to the curves reported by Boyer et al. (2011). For ω= 1 rad/s and g_s = 0.40, 0.42, and 0.44, two sets of data points are shown. The lower data points correspond to d= 0.58 mm and $\eta_\ell^0 = 2.15$ Pa s, whereas the upper points were obtained for d= 1.1 mm and $\eta_\ell^0 = 3.1$ Pa s. These findings are discussed in the following section.

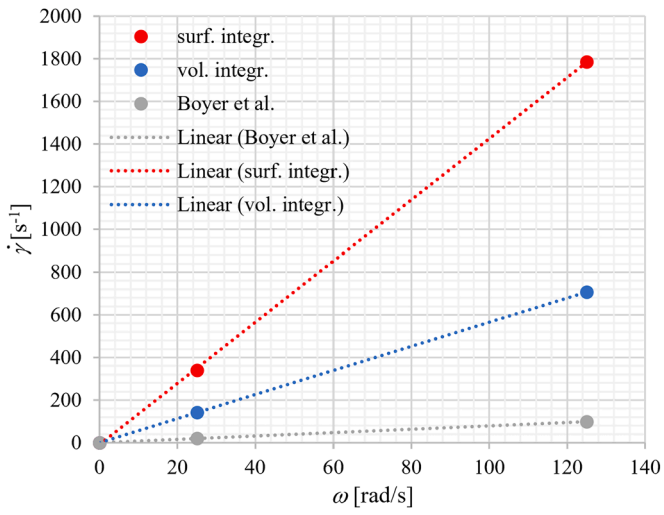

Fig. 2. Shear rate as a function of rotation speed, estimated from the surface integration directly beneath the annulus, Eq. (10), from the volume integration over the entire domain, Eq. (13), and using the simplified approach proposed by Boyer et al. (2011).

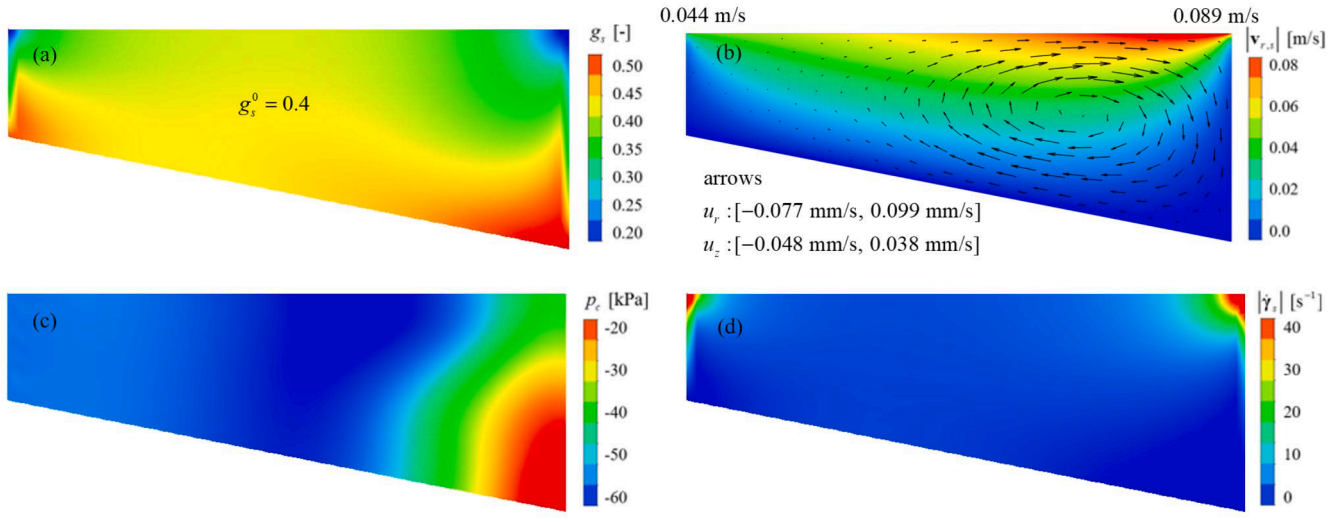

Fig. 3. Example for a simulated case with g_s^0= 0.40, ω= 1 rad/s (0.16 s^{-1} ≈ 9.5 rpm), d= 0.58 mm and η_ℓ^0= 2.15 Pa·s showing (a) volume fraction, (b) particle velocity magnitude (colours) and particle axial-radial velocity (arrows), (c) particle pressure, and (d) particle shear rate. The axial-radial velocity ranges from -0.077 to +0.099 m/s for the radial component and from -0.048 to +0.038 m/s for the axial component.

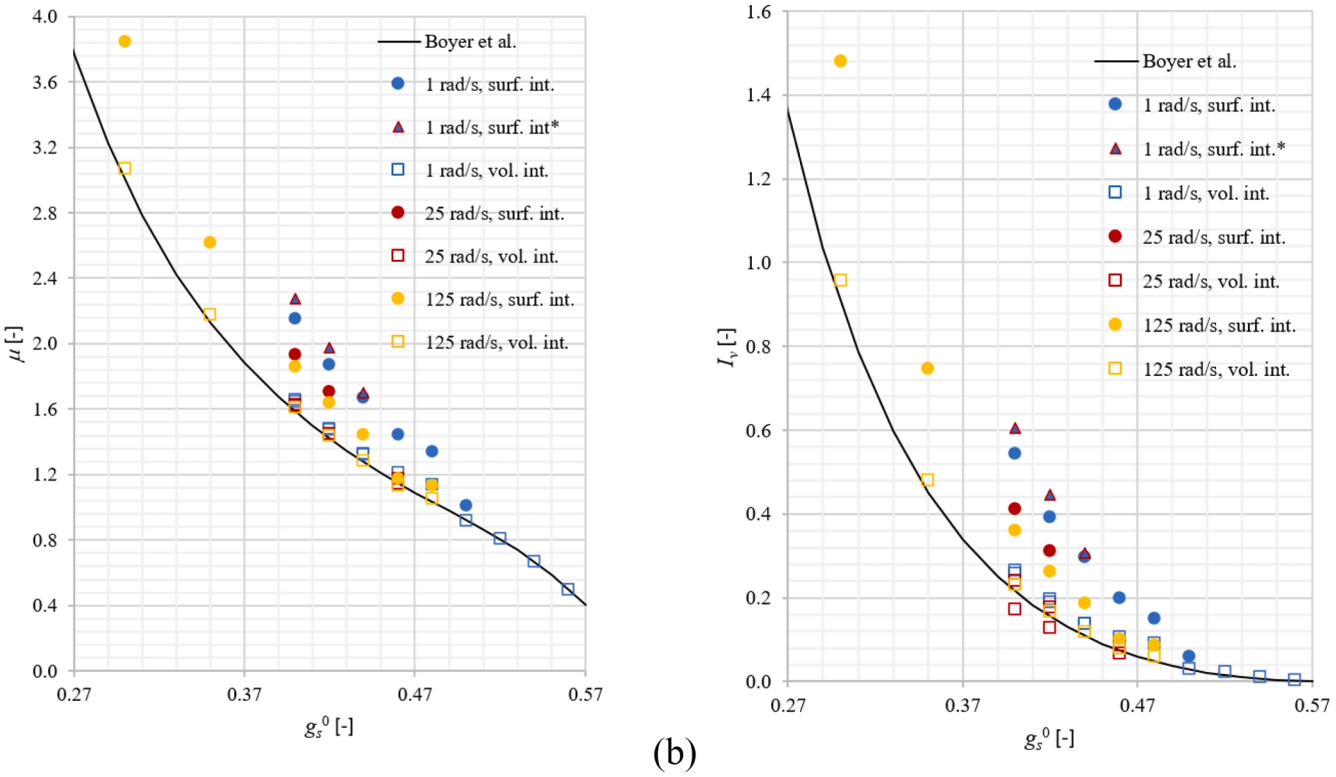

Fig. 4. Friction coefficient (a) and dimensionless viscous number (b) as functions of the solid volume fraction for different rotation speeds, ω, determined from $\overline{\tau}_{surf}$,$\overline{p}_{c,surf}$, and $\overline{\dot{\gamma}}_{surf}$ (surface integration, Eqs. (8-10)), from $\overline{\tau}_{vol}$, $\overline{p}_{c,Vol}$ and $\overline{\dot{\gamma}}_{vol}$ (volume integration, Eqs. (11-13)), and from the application of Eqs. (6-7) following Boyer et al. (2011). All simulations were done for d= 0.58 mm and η_ℓ^0 = 2.15 Pa s, except those labeled with the asterisks, where d= 1.1 mm and η_ℓ^0 = 3.1 Pa s was used.

4. Discussion

In the volume-average Euler-Euler simulation, the shear rates, $\overline{\dot{\gamma}}_{surf}$ and $\overline{\dot{\gamma}}_{vol}$, are predominantly governed by the different boundary conditions at the inner and outer upper edges of the shear cell, where the cell remains fixed while the annulus rotates. In the experiment, a small gap between the annulus and the cell wall may allow for a smoother transition in velocity from zero to the rotation speed. This would certainly reduce the extremely high shear rates predicted at the inner and outer edges between the annulus and the cell walls. Boyer et al. (2011) completely ignored this "edge-effect" by assuming a linear velocity profile between the rotating annulus and the bottom of the cell, resulting in a constant and relatively small shear rate that depends on the mean depth of the rheometer cell. Although the presented numerical model still has limitations in accurately reproducing reality, elevated shear rates at the upper edges are still expected.

Self-evidently, the numerically estimated values of $\bar{\dot{\gamma}}_{surf}$ and $\bar{\dot{\gamma}}_{vol}$ also increase linearly with ω, just as $\dot{\gamma}_B$ does (Fig. 2). Both integrations, $\bar{\dot{\gamma}}_{surf}$ and $\bar{\dot{\gamma}}_{vol}$, account not only for the high corner values of $\dot{\gamma}$ but also for the smaller values in the bulk. Since the proportion of these smaller bulk values is much larger in the volume integration than in the surface integration, the resulting $\bar{\dot{\gamma}}_{vol}$ is smaller than $\bar{\dot{\gamma}}_{surf}$.

It is important to note that the results presented in Fig. 3 represent a typical experiment presented in Boyer et al. (2011), however, at relative moderate initial solid volume fraction of $g_s^0 = 0.40$. A distinct difference is that the simulation was performed under volume-imposed conditions, whereas the experiment was carried out under pressure-imposed conditions. While pressure-imposed and volume-imposed tests are not inherently equivalent, particularly during transient evolution, they should exhibit similar steady-state characteristics. In the present work, the volume-imposed formulation is therefore used as a numerical surrogate to infer steady-state spatial distributions, while acknowledging that a strict equivalence with pressure-imposed experiments cannot be established within the scope of this study.

It is also worth noting that our numerical results suggest how a specific rheometric geometry may influence the redistribution of local fields when analyzed using a two-phase model with particle pressure. Since these fields have not been directly validated against experimental data, they should not be interpreted as established physical truth.

The high shear rate values of the solid phase at the upper corners of the domain turn out to be one of the most important features influencing the overall dynamics in the cell. As already mentioned, they arise from the different boundary conditions imposed at the annulus and at the side walls. At the annulus boundary, both the particles and the liquid move with the rotation speed of the annulus. In contrast, at the side wall boundaries, the particles are permitted to slip while the liquid remains at rest.

For the liquid located directly at the corner, the discontinuous change from zero velocity at the wall to the circumferential velocity at the annulus generates a large shear rate at the upper inner edge of the cell and an even higher one at the upper outer edge. It is evident that the greater the rotation speed, the larger the shear rate of the liquid at the edges. Under steady-state conditions, the discontinuous jump in the liquid velocity is likewise transmitted to the solid phase.

In a real experiment, the boundary condition for the solid phase may differ from the assumption adopted in the present model. Varsakelis et al. (2022) showed that the relationship between the required slip and the average solid fraction is more complex than that predicted by classical slip boundary condition formulations. Experimental studies of particle concentration in channel flows of dense suspensions indicate that imposing a no-slip boundary condition on the granular phase velocity is inconsistent with observations and instead suggests the presence of a slip layer.

Numerical simulations tend to overestimate the solid volume fraction because, in the absence of sufficient slip, particle migration is hindered. However, a more sophisticated treatment of the boundary conditions for the solid phase is beyond the scope of the present work. The results presented here should therefore be interpreted as an informative representation of the process rather than an exact reproduction of physical reality. Nevertheless, even when accounting for reduced slip of the solid particles at the cell walls, large gradients in the solid velocity would still occur at the edges. Consequently, the qualitative discussion presented here remains valid.

The no-slip boundary conditions imposed on both phases at the base result in an almost zero velocity for both the particles and the liquid in the near-bottom region. As a result, the particle velocity profile shown in Fig. 3 deviates significantly from the one-dimensional assumption adopted in Boyer et al. (2011). The reason for that is that the no-slip boundary condition imposed on the liquid at the walls also reduces the particle velocity in the near-wall regions, resulting in a more two-dimensional axial particle velocity field. The only way to obtain a strictly one-dimensional velocity field in the simulation is to impose slip boundary conditions for both phases at the inner and outer walls. Although this assumption is physically unrealistic, we have verified it for completeness.

In the case shown in Fig. 3, the elevated shear-rate values in the upper corners give rise to pronounced shear rate gradients and, according to Eqs. (4–5), to significant gradients in both particle pressure and shear stress. These gradients directly influence the solid-phase momentum balance, as described by Eq. (22). Consequently, the solid phase is expelled from the upper edges of the cell, and at the upper outer edge, deflected downwards. This mechanism provides the driving force for the clockwise particle axial-radial flow observed in Fig. 3.

Large shear-stress gradients at the upper edges, resulting from pronounced shear rate gradients, would also arise even if particle pressure were neglected. Fig. 5 presents the corresponding simulation results for the same case as shown in Fig. 3, but without accounting for particle pressure. An particle axial-radial flow is again predicted by the model; however, its intensity is significantly reduced.

Another important phenomenon that arises from our volume-averaged Euler–Euler approach is the non-uniform distribution of solid volume fraction within the domain. In the simulation, the high particle pressure in the upper corners, particularly in the upper outer corner, drives the migration of particles away from these regions. The model predicts that through the axial-radial flow, they are transported from the upper corners into the bulk and ultimately accumulate in the lower corners. When the solid volume fraction approaches the packing limit, the particles cease to flow because the effective solid viscosity increases by several orders of magnitude compared with the value corresponding to the initial value of $g_s^0 = 0.40$. Consequently, $\dot{\gamma}$ becomes relatively small in the lower outer corner, and therefore, the particle pressure shown in Fig. 3 is minimal there.

Using the same argument, the model predicts that, in the case with particle pressure, the high $\dot{\gamma}$ do not extend as far downwards as in the case without particle pressure. The simulated velocity is affected by the predicted solid fraction distribution: as the solid fraction increases at the bottom corners in the case with particle pressure, the viscosity increases, and the solid velocity gradient at the bottom is reduced (i.e., a larger bluish area is predicted in the case with particle pressure than in the case without it).

The discussion presented so far provides insight into mechanisms that lead to the results shown in Figs. 3 and 5. Their importance and relative strength may vary when the imposed rotation rate or the initial volume fraction is changed.

Before discussing the results presented in Fig. 4, it should be noted that Boyer's curves for $\mu - g_s$ and $I_v - g_s$ are, in fact, equivalent to the $\eta_s - g_s$ and $\eta_n - g_s$ relationships used as input to Eqs. (4–5) in the simulation. Consequently, reproducing the $\mu - g_s$ and $I_v - g_s$ curves by the numerical simulations merely reflects the fact that the model yields what has been prescribed as input. This is the reason why μ_{Vol} and $I_{v,Vol}$ approximately reproduce Boyer's curves, although the values of $\bar{\dot{\gamma}}_{vol}$ estimated numerically are, as shown in Fig. 2, considerably larger than those of $\dot{\gamma}_B$.

As outlined above, the corresponding friction coefficient is given by $\mu_{Vol} = \bar{\tau}_{Vol}/\bar{P}_{c,Vol}$, and the dimensionless viscosity number by $I_{v,Vol} = \eta_\ell^0 \bar{\dot{\gamma}}_{Vol}/\bar{P}_{c,Vol}$. From the latter relationship, it follows that the good agreement between $I_{v,Vol}$ and Boyer's curve is only possible if $\bar{P}_{c,Vol}$ scales with $\bar{\dot{\gamma}}_{Vol}$. This can be understood from the fact that the integrands in both integral expressions, Eqs. (12–13), are linked via the solid-phase viscosity (Eq. (5)). The same reasoning applies to μ_{Vol}, since the integrand in the corresponding integral expression for $\bar{\tau}_{Vol}$ (Eq. (11)) is likewise connected to that of $\bar{\dot{\gamma}}_{Vol}$ through the solid-phase viscosity. In other words, $\mu_{Vol}(g_s^0)$ and $I_{v,Vol}(g_s^0)$ must coincide with Boyer's curve, since they are obtained from the input of the corresponding $\eta_s - g_s$ and $\eta_n - g_s$ relationships.

It is interesting to note that μ_{Vol} and $I_{v,Vol}$ are independent of the

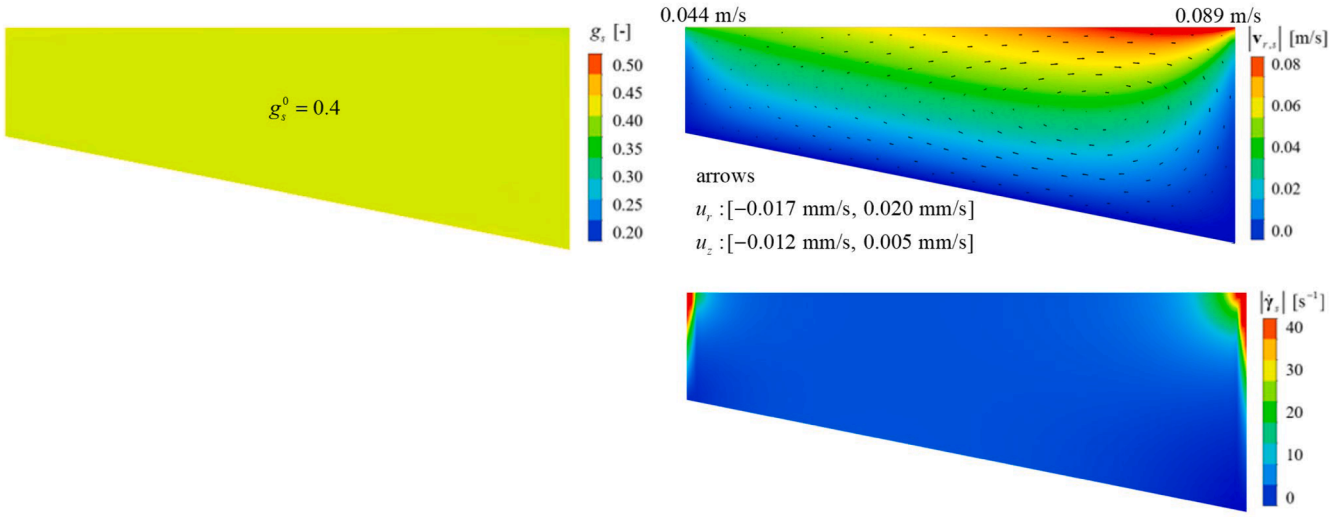

Fig. 5. Simulation results for similar case as that shown in Fig. 2, but without considering the particle pressure. The axial-radial velocity now ranges from -0.017 to +0.020 m/s for the radial and from -0.012 to +0.005 m/s for the axial components.

actual processes occurring locally within the domain, because $\overline{\tau}_{\mathrm{Vol}}$, $\overline{P}_{c,\mathrm{Vol}}$, and $\overline{\dot{\gamma}}_{\mathrm{Vol}}$ depend in the same manner on the local variations of $\dot{\gamma}_s$and g_s. This is not the case for $\overline{\tau}_{\mathrm{surf}}$, $\overline{P}_{c,surf}$, and $\overline{\dot{\gamma}}_{\mathrm{surf}}$, and consequently not for μ_{surf} and $I_{v,\mathrm{surf}}$. For these quantities, processes affecting τ, P_c, and $\dot{\gamma}$ along the annulus are of crucial importance.

For example, at $g_s^0 = 0.40$ and $\omega = 1$ rad/s, with $d = 0.58$ mm and $\eta_\ell^0 = 2.15$ Pa s (Fig. 3), we obtain $\overline{P}_{c,\mathrm{surf}} = 52.7$ Pa. In contrast, for $d = 1.1$ mm and $\eta_\ell^0 = 3.1$ Pa s, the result is $\overline{P}_{c,\mathrm{surf}} = 68.3$ Pa. The value of $\overline{\dot{\gamma}}_{\mathrm{surf}}$ is identical in both cases. Evidently, $\overline{P}_{c,\mathrm{surf}}$ increases predominantly due to the higher viscosity of the suspending liquid, η_ℓ^0. This is also reflected in the mean shear stress along the annulus, with $\overline{\tau}_{\mathrm{surf}} = 113.4$ Pa for the first case and $\overline{\tau}_{\mathrm{surf}} = 155.6$ Pa for the second. Although the ratio $\overline{\dot{\gamma}}_{\mathrm{surf}} / \overline{P}_{c,\mathrm{surf}}$ is larger for the first case, the value of $I_{v,\mathrm{surf}} = \eta_\ell^0 \overline{\dot{\gamma}}_{\mathrm{surf}} / \overline{P}_{c,\mathrm{surf}}$ remains smaller because η_ℓ^0 prevails. This is illustrated in Fig. 4 when comparing the data points for $g_s^0 = 0.40$ and $\omega = 1$ rad/s (with and without asterisk).

For $\mu_{\mathrm{surf}} = \overline{\tau}_{\mathrm{surf}} / \overline{P}_{c,\mathrm{surf}}$, we obtain a slightly larger value of μ_{surf} in the second case than in the first. Although both quantities, $\overline{P}_{c,\mathrm{surf}}$ and $\overline{\tau}_{\mathrm{surf}}$, increase when a higher viscosity of the suspending liquid, η_ℓ^0, is considered, $\overline{\tau}_{\mathrm{surf}}$ increases slightly more than $\overline{P}_{c,\mathrm{surf}}$. The reason lies in the different dependence on solid volume fraction of the two viscosities, η_s (relevant for $\overline{\tau}_{\mathrm{surf}}$) and η_n (relevant for $\overline{P}_{c,\mathrm{surf}}$). This becomes significant because the mean solid volume fraction along the annulus is $\overline{g}_{s,\mathrm{surf}} = 0.366$ for the first case and $\overline{g}_{s,\mathrm{surf}} = 0.359$ for the second case. This difference, in turn, results from the larger values of $\overline{P}_{c,\mathrm{surf}}$ and $\overline{\tau}_{\mathrm{surf}}$, which drive the clockwise axial-radial flow somewhat stronger and consequently transport slightly more particles away from the annulus. Similar arguments can be found for the other two sets of data points for $\omega = 1$rad/s and $g_s^0 = 0.42$, and 0.46 (with and without asterisk).

In general, $\overline{P}_{c,\mathrm{surf}}$ and $\overline{\tau}_{\mathrm{surf}}$ increase more rapidly with ω than $\overline{\dot{\gamma}}_{\mathrm{surf}}$. This is because, with increasing rotational speed, the formation of the clockwise flow becomes progressively more difficult. As a result, the solid volume fraction along the annulus, $\overline{g}_{s,\mathrm{surf}}$, remains closer to the initially imposed solid volume fraction, g_s^0. This, in turn, leads to an increase in η_n and η_s, thereby explaining the disproportionate growth of $\overline{P}_{c,\mathrm{surf}}$ and $\overline{\tau}_{\mathrm{surf}}$ compare to $\overline{\dot{\gamma}}_{\mathrm{surf}}$.

According to Fig. 4, for increasing g_s^0, the values of μ_{surf} and $I_{v,\mathrm{surf}}$ approach those of μ_{Vol}, and $I_{v,\mathrm{Vol}}$. At $g_s^0 = 0.50$, which is the largest initial solid fraction for which a reliable steady state could be obtained, these values are already quite close. Under these conditions, the clockwise axial-radial flow becomes weak and $\overline{g}_{s,\mathrm{surf}}$ remains nearly equal to g_s^0.

For a larger initial solid fraction, the numerical scheme became increasingly unstable, and reliable steady-state results could no longer be obtained. Although smaller time steps generally improve convergence, the increase of η_s and η_n by several orders of magnitude ultimately creates an imbalance among the different terms in the conservation equations, pushing the numerical scheme to its limits.

The values of μ_{Vol} and $I_{v,\mathrm{Vol}}$ for $g_s^0 \geq 0.50$ shown in Fig. 4 were obtained without achieving reliable steady-state conditions. Therefore, we did not show the corresponding values of μ_{surf} and $I_{v,\mathrm{surf}}$. As said previously, μ_{Vol} and $I_{v,\mathrm{Vol}}$ are independent of the actual processes occurring locally within the domain, even when these processes are numerical artefacts. They merely reflect the $\eta_s - g_s$ and $\eta_n - g_s$ relationships used as input.

Although not directly proven by our simulations, it stands to reason that as g_s^0 approaches the packing limit, even a very large $\dot{\gamma}$ in the upper outer corner (larger ω) is no longer sufficient to deflect the particles downwards. Consequently, the clockwise axial-radial flow no longer occurs, and $\overline{g}_{s,\mathrm{surf}}$ remains essentially at g_s^0. Under such conditions, the distinction between μ_{surf} and μ_{Vol}, as well as between $I_{v,\mathrm{surf}}$ and $I_{v,\mathrm{Vol}}$, becomes obsolete.

5. Conclusions

The presented two-phase, volume-averaged model enables the prediction of process details that would otherwise remain obscure. Its application to a rotational annular shear cell rheometer suggests the conditions under which commonly made simplifications are justified. The use of a volume-imposed formulation represents a pragmatic modeling choice necessitated by numerical constraints. A more rigorous assessment of the relationship between pressure-imposed and volume-imposed conditions in this geometry would require dedicated investigation and is left for future work.

For a rheological shear cell experiment such as the one considered here, the most critical phenomenon governing the entire process is the development of a high shear rate along the upper outer edge of the cell. Although the numerical model does not account for the small gap between annulus and cell wall, and more sophisticated boundary conditions for the particles at the cell walls may be necessary, it is reasonable to expect a high shear rate to arise because the suspending liquid is forced to rotate with the annulus while remaining stationary at the cell walls. Under steady-state conditions, the particle phase adopts this elevated shear rate.

The shear stress and the particle pressure are linear functions of the

shear rate: the shear stress through the shear viscosity, and the particle pressure through the normal viscosity. In the upper outer corner region, both quantities increase linearly with the rotation speed via the shear rate, and highly non-linearly with the applied solid volume fraction through the two viscosities.

High shear stresses and particle pressures at the upper outer edge also give rise to correspondingly large gradients. These gradients, in turn, are predicted to generate an axial-radial flow from smaller to larger radii that is superimposed on the global rotation flow. By comparing simulations with and without particle pressure, it can be shown that the strength of this axial-radial flow is determined primarily by the particle pressure. The anisotropic structure of the particle pressure further influences the directional character of the migration process.

The axial-radial flow has two important implications. Firstly, it transports particles from the area beneath the annulus towards the bottom region of the cell, thereby generating a non-uniform distribution of solid volume fraction. Secondly, quantities such as particle pressure, shear stress, and shear rate, when integrated over the surface of the annulus, depend on the particle redistribution. These integrals are crucial for comparing simulation results with experimental measurements.

It was discussed that the friction coefficient, μ, and the dimensionless viscosity number, I_v, are independent of the rotation speed if the strength of the axial-radial flow is negligibly small and no particle redistribution occurs. This should happen only for a large enough applied particle volume fraction. Then, the corresponding surface-integrated quantity of particle pressure and shear stress scales linearly with that of the shear rate.

It is one of the most striking findings of the present work that the scaling of particle pressure and shear stress with the shear rate allows for correct measurements of μ and I_v, even when the numerically estimated shear rates deviate substantially from the values considered in the experiments. The commonly assumed linear decrease in rotational velocity from the annulus to the base, on which the 'measured' shear rate value is typically based, seems most likely to be incorrect. The non-slip boundary conditions for the liquid phase at the cell walls give rise to a more two-dimensional axial-radial velocity profile rather than a one-dimensional one. Our simulations suggest that the shear rate may in fact be several times larger than that implied by the oversimplified assumption used in the interpretation of the experimental measurements.

CRediT authorship contribution statement

A. Ludwig: Writing – review & editing, Writing – original draft, Validation, Supervision, Project administration, Methodology, Funding acquisition, Formal analysis, Conceptualization. **C. Gomes Rodrigues:** Writing – review & editing, Software, Methodology, Investigation, Formal analysis, Data curation. **M. Stefan-Kharicha:** Investigation. **M. Wu:** Validation. **A. Kharicha:** Validation.

Declaration of competing interest

The authors declare that they have no known competing financial interests or personal relationships that could have appeared to influence the work reported in this paper.

Acknowledgement

We gratefully acknowledge financial support from the Austrian Science Fund (FWF) under grant DOI https://doi.org/10.55776/P34993.

Data availability

Data will be made available on request.

References

Ahnert, T., Münch, A., Wagner, B., 2019. Models for the two-phase flow of concentrated suspensions. Eur. J. Appl. Math. 30, 585–617. https://doi.org/10.1017/S095679251800030X.

Boyer, F., Guazzelli, E., Pouliquen, O., 2011. Unifying suspension and granular rheology. Phys. Rev. Lett. 107, 188301. https://doi.org/10.1103/PhysRevLett.107.188301.

Cai, D., Ren, F., Ge, H., Kim, H.S., Li, J., Li, J., 2019. Modelling of inclusion effects on macrosegregation in solidifying steel ingot with a multi-phase approach. Metall. Mater. Trans. A Phys. Metall. Mater. Sci. 50, 1323–1332. https://doi.org/10.1007/s11661-018-5066-5.

Combeau, H., Založnik, M., 2014. Multiphysics and multiscale models in modeling and simulation of solidification processes. In: Massarotti, N., Nithiarasu, P., Šarler, B. (Eds.), ThermaComp, 2014.

Combeau, H., Založnik, M., Hans, S., Richy, P.E., 2009. Prediction of macrosegregation in steel ingots: influence of the motion and the morphology of equiaxed grains. Met. Mater. Trans. B 40, 289–304. https://doi.org/10.1007/s11663-008-9178-y.

Dantzig, J.A., Rappaz, M., 2016. Solidification, 2nd ed. EPFL Press.

Farup, I., Mo, A., 2000. Two-phase modeling of Mushy zone parameters associated with hot tearing. Met. Mater. Trans. A 31, 1461–1472. https://doi.org/10.1007/s11661-000-0264-2.

Ge, H., Ren, F., Li, J., Han, X., Xia, M., Li, J., 2017. Four-phase dendritic model for the prediction of macrosegregation, shrinkage cavity, and porosity in a 55-ton ingot. Met. Mater. Trans. A 48, 1139–1150. https://doi.org/10.1007/s11661-016-3910-z.

Ge, H., Ren, F., Li, J., Hu, Q., Xia, M., Li, J., 2018. Modelling of ingot size effects on macrosegregation in steel castings. J. Mater. Process. Technol. 252, 362–369. https://doi.org/10.1016/j.jmatprotec.2017.09.004.

Gu, J.P.P., Beckermann, C., 1999. Simulation of convection and macrosegregation in a large steel ingot. Met. Mater. Trans. A 30, 1357–1366. https://doi.org/10.1007/s11661-999-0284-5.

Guazzelli, É., Pouliquen, O., 2018. Rheology of dense granular suspensions. J. Fluid Mech. 852, 1–73. https://doi.org/10.1017/jfm.2018.548.

Heyvaert, L., Bedel, M., Založnik, M., Combeau, H., 2017. Modeling of the coupling of microstructure and macrosegregation in a direct chill cast Al-Cu billet. Met. Mater. Trans. A 48, 4713–4734. https://doi.org/10.1007/s11661-017-4238-z.

Krieger, I.M., 1972. Rheology of monodisperse latices. Adv. Colloid Interface Sci. 3, 111–136. https://doi.org/10.1016/0001-8686(72)80001-0.

Krieger, I.M., Dougherty, T.J., 1959. A mechanism for non-Newtonian flow in suspensions of rigid spheres. Trans. Soc. Rheol. 3, 137–152. https://doi.org/10.1122/1.548848.

Leriche, N., Combeau, H., Gandin, C.-A., Založnik, M., 2015. Modelling the columnar-to-equiaxed and equiaxed-to-columnar transitions in ingots using a multiphase model. IOP Conf. Ser. Mater. Sci. Eng. 84, 012087. https://doi.org/10.1088/1757-899X/84/1/012087.

Li, J., Wu, M., Ludwig, A., Kharicha, A., 2014. Simulation of macrosegregation in a 2.45-ton steel ingot using a three-phase mixed columnar-equiaxed model. Int. J. Heat Mass Transf. 72, 668–679. https://doi.org/10.1016/j.ijheatmasstransfer.2013.08.079.

Ludwig, A., Kharicha, A., Wu, M., 2014. Modeling of multiscale and multiphase phenomena in materials processing. Met. Mater. Trans. B 45, 36–43. https://doi.org/10.1007/s11663-013-9820-1.

Ludwig, A., Rodrigues, C.M.G., Wu, M., Kharicha, A., 2020. Modelling of shear bands during solidification. IOP Conf. Ser. Mater. Sci. Eng. 861, 012066. https://doi.org/10.1088/1757-899X/861/1/012066.

Ludwig, A., Wu, M., 2002. Modeling of globular equiaxed solidification with a two-phase approach. Met. Mater. Trans. A 33, 3673–3683. https://doi.org/10.1007/s11661-002-0241-z.

Lyon, M.K., Leal, L.G., 1998. An experimental study of the motion of concentrated suspensions in two-dimensional channel flow. Part 1. Monodisperse systems. J. Fluid Mech. 363, 25–56. https://doi.org/10.1017/S0022112098008817.

Martin, C.L., Braccini, M., Suery, M., 2002. Rheological behavior of the mushy zone at small strains. Mater. Sci. Eng. A 325, 292–301. https://doi.org/10.1016/S0921-5093(01)01528-3.

Martin, C.L., Favier, D., Suery, M., 1999. Fracture behaviour in tension of viscoplastic porous metallic materials saturated with liquid. Int. J. Plast. 15, 981–1008.

Martin, C.L., Favier, D., Suery, M., 1997a. Viscoplastic behaviour of porous metallic materials saturated with liquid part I: constitutive equations. Int. J. Plast. 13, 237–259. https://doi.org/10.1016/S0749-6419(97)00010-7.

Martin, C.L., Favier, D., Suery, M., 1997b. Viscoplastic behaviour of porous metallic materials saturated with liquid, Part II: experimental identification on a Sn-Pb model alloy. Int. J. Plast. 13, 237–259. https://doi.org/10.1016/S0749-6419(97)00010-7.

Morris, J.F., Boulay, F., 1999. Curvilinear flows of noncolloidal suspensions : the role of normal stresses. J. Rheol. (N. Y. N. Y). 43, 1213–1237. https://doi.org/10.1122/1.551021.

Nguyen, T.G., Favier, D., Suery, M., 1994. Theoretical and experimental study of the isothermal mechanical behaviour of alloys in the semi-solid state. Int. J. Plast. 10, 663–693.

Nguyen, T.T., Gandin, C.-A., Combeau, H., Zaloznik, M., Bellet, M., 2018. Finite element multi-scale modeling of chemical segregation in steel solidification taking into account the transport of equiaxed grains. Met. Mater. Trans. A online. 49, 1725–1748. https://doi.org/10.1007/s11661-018-4496-4.

Nguyen, T.T.M., Combeau, H., Zalodnik, M., Bellet, M., Gandin, C.-A., 2015. Multi-scale Unite element modelling of solidification structures by a splitting method taking into account the transport of equiaxed grains. IOP Conf. Ser. Mater. Sci. Eng. 84, 012007. https://doi.org/10.1088/1757-899X/84/1/012007.

Ni, J., Beckermann, C., 1993. Modeling of globulitic alloy solidification with convection. J. Mater. Process. Manuf. Sci.

Ni, J., Beckermann, C., 1991. A volume-averaged two-phase model for transport phenomena during solidification. Met. Trans. B 22, 349–361. https://doi.org/10.1007/BF02651234.

Phillips, R.J., Armstrong, R.C., Brown, R.A., Graham, A.L., Abbott, J.R., 1992. A constitutive equation for concentrated suspensions that accounts for shear-induced particle migration. Phys. Fluids A 4, 30–40. https://doi.org/10.1063/1.858498.

Ren, F., Ge, H., Cai, D., Li, Jun, Hu, Q., Xia, M., Li, Jianguo, 2018. Simulation of macrosegregation and shrinkage cavity in an Al-4.5 Wt Pct Cu ingot using a four-phase model. Metall. Mater. Trans. A Phys. Metall. Mater. Sci. 49, 6243–6254. https://doi.org/10.1007/s11661-018-4892-9.

Varsakelis, C., Gelbgras, V., Papalexandris, M.V, 2022. On the wall boundary condition for the velocity in concentrated suspensions. J. Nonnewton. Fluid Mech. 305, 104830. https://doi.org/10.1016/j.jnnfm.2022.104830.

Wang, Z., Luo, S., Wang, W., Zhu, M., 2020. Numerical simulation of solidification structure of continuously cast billet with grain motion. Met. Mater. Trans. B 51, 2882–2894. https://doi.org/10.1007/s11663-020-01953-2.

Wu, M., Fjeld, A., Ludwig, A., 2010a. Modelling mixed columnar-equiaxed solidification with melt convection and grain sedimentation–Part I: model description. Comp. Mater. Sci. 50, 32–42. https://doi.org/10.1016/j.commatsci.2010.07.005.

Wu, M., Ludwig, A., 2009a. Modeling equiaxed solidification with melt convection and grain sedimentation-I: model description. Acta Mater. 57, 5621–5631. https://doi.org/10.1016/j.actamat.2009.07.056.

Wu, M., Ludwig, A., 2009b. Modeling equiaxed solidification with melt convection and grain sedimentation - II . model verification. Acta Mater. 57, 5632–5644. https://doi.org/10.1016/j.actamat.2009.07.067.

Wu, M., Ludwig, A., Fjeld, A., 2010b. Modelling mixed columnar-equiaxed solidification with melt convection and grain sedimentation–Part II: illustrative modelling results and parameter studies. Comp. Mater. Sci. 50, 43–58. https://doi.org/10.1016/j.commatsci.2010.07.006.

Wu, M., Ludwig, A., Kharicha, A., 2018. Simulation of As-cast steel ingots. Steel Res. Int. 89 (1700037), 1–14. https://doi.org/10.1002/srin.201700037.

Wu, M., Ludwig, A., Kharicha, A., 2017. A four phase model for the macrosegregation and shrinkage cavity during solidification of steel ingot. Appl. Math. Model. 41, 102–120. https://doi.org/10.1016/j.apm.2016.08.023.

Založnik, M., Combeau, H., 2010. Thermosolutal flow in steel ingots and the formation of mesosegregates. Int. J. Therm. Sci. 49, 1500–1509. https://doi.org/10.1016/j.ijthermalsci.2010.04.011.